

# Mechanical Behaviors and Failure Analysis of S38C Steel with Gradient Structure Fabricated by Induction Heating and Quenching

Gen Li, Liting Zeng, Qingqing Jiang, Yao Wang, Rubing Guo, and Zhiwei Ma\*

This article proposes a simple and fast method of induction heating and quenching to produce surface gradient structure for S38C steel, and its mechanical behavior and strengthening mechanism are revealed. The variation of the gradient structure from surface to interior is characterized by electron backscatter diffraction, and the tensile behavior of the gradient structure at different depths is acknowledged by the small-scale tensile tests. The gradient structure is tempered martensite microstructure, which significantly improves the hardness and tensile strength of surface and subsurface regions. Accordingly, with the strengthening of the gradient structure, the general tensile strength and fatigue behavior of the S38C steel are increased close to those of high-strength steel. Moreover, the fatigue crack initiation mechanism of the gradient structure is studied by energy dispersive spectroscopy, transmission Kikuchi diffraction, and transmission electron microscope characterization on the crack initiation regions. It reveals that the fatigue failure of the gradient structure can be due to stress concentration on the surface and around subsurface inclusions, and the crack initiation modes present surface crack initiation and internal crack initiation, respectively.

such a high-strength gradient structure could effectively improve the surface loading capacity as well as inhibit surface crack initiation and growth.<sup>[15]</sup> Different from those advanced and expensive high-strength materials with complicated fabrication processes, the fabrication of gradient structure could use engineering materials to achieve good mechanical performance and has the advantages of relatively low expense and operating flexibility.<sup>[9]</sup> Therefore, this strengthening strategy is popular for the components and materials that require high strength and good fatigue resistance as well as low cost, e.g., for S38C steel used in high-speed railway axles.<sup>[10,11]</sup>


Researchers have explored many methods to produce surface gradient structures and improve mechanical behaviors in the last decades, including induction heating,<sup>[15–18]</sup> shot peening,<sup>[19]</sup> predeformation,<sup>[1]</sup> surface mechanical attrition,<sup>[20]</sup> surface mechanical grinding,<sup>[21]</sup> and salt-bath heat treatment.<sup>[22]</sup> The thickness of gradient structures could be varied from hundreds of nanometers to millimeters.<sup>[15]</sup> Fang et al.<sup>[23]</sup> and Lu<sup>[7]</sup> introduced a gradient nano-grained (GNG) Cu film on a coarse-grained (CG) Cu substrate material through surface mechanical grinding treatment (SMGT). The treated material with a gradient structure got a much higher tensile strength than that of CG Cu substrate and did not lose too much ductility. By introducing the gradient structure on GNG/CG Cu samples through SMGT method, Yang et al.<sup>[24]</sup>

## 1. Introduction

Introducing surface gradient structure is fabricating a layer of high-strength structure on a material surface, and this strengthening strategy has been widely used in metallic materials and components to improve their mechanical performance,<sup>[1,2]</sup> including tensile strength,<sup>[3–5]</sup> fracture toughness,<sup>[6]</sup> ductility,<sup>[7]</sup> fatigue strength,<sup>[8–13]</sup> and friction behavior.<sup>[14]</sup> Moreover, since cracks usually initiate from the material surface, introducing

G. Li  
Department of Mechanics  
School of Physical Science and Engineering  
Beijing Jiaotong University  
Beijing 100044, China

L. Zeng, Z. Ma  
State Key Laboratory of Nonlinear Mechanics  
Institute of Mechanics  
Chinese Academy of Sciences  
Beijing 100190, Beijing, China  
E-mail: mzw@lnm.imech.ac.cn

 The ORCID identification number(s) for the author(s) of this article can be found under <https://doi.org/10.1002/srin.202300384>.

DOI: 10.1002/srin.202300384

Q. Jiang  
Huawei Digital Power Technologies Co., Ltd.  
Xi'an 710075, Shaanxi Province, China

Y. Wang  
Beijing Institute of Astronautical Systems Engineering  
Beijing 100076, Beijing, China

R. Guo  
State Key Laboratory of Rail Transit Vehicle System  
Southwest Jiaotong University  
Chengdu 610031, Sichuan Province, China

Z. Ma  
Branch of Vanadium and Titanium Research Institute  
Ansteel Beijing Research Institute Co., Ltd.  
Future Science Park, Beijing 102209, Beijing, China

revealed substantial enhancement in fatigue strength (from 56 to 98 MPa), and surface crack nucleation was suppressed. Roland et al.<sup>[25]</sup> studied the surface mechanical attrition treatment method and the gradient structure exhibited a great improvement in fatigue life in low cycle fatigue and high cycle fatigue (HCF) regimes. Liu et al.<sup>[26]</sup> compared induction heating and quenching with shot peening on EA4T axle steel and reported that the former treatment had a better effect on the increase of fatigue strength. Therefore, the exploration of the different treatment methods to improve mechanical performance of engineering materials is meaningful. Among these methods, the method of induction heating and quenching has the advantages of lower cost and simple implementation,<sup>[27]</sup> while the challenge is that the specific process parameters (such as frequency and time) and the corresponding mechanical properties are still unclear.

The strengthening mechanism of the gradient structure is essential for understanding the strengthening capacity, and previous studies<sup>[28–30]</sup> have reported some mechanisms based on microscopic studies. Ma et al.<sup>[28]</sup> studied an austenitic stainless steel with gradient structure, and found that the stress partition is optimized in the gradient structure. The hard martensitic structure suffers high loading and the soft austenitic phase keeps substantial tensile ductility. Wu et al.<sup>[4]</sup> adopted a strain-hardening mechanism for their gradient structure, which achieved high strength and good ductility. In their research, the grain-size gradient under tension could induce strain gradient and further promote dislocation accumulation and interaction, which lead to extra strain hardening. Moreover, some treatments<sup>[15,25]</sup> for fabricating gradient structures also could produce residual compressive stress around the surface, which could effectively resist the propagation of surface cracks.

The medium carbon steel S38C is commonly used in axles of high-speed railways. Since the axles are large structural parts and the surface of the axles is a main area subjected to high stress and crack initiation, it demands to introduce surface hardening layer of about 3 mm to improve local strength and hardness, inhibit surface crack initiation, and prolong service life. Therefore, it is essential to explore the method to produce a surface gradient structure for the axles and understand the mechanical behavior and fatigue performance of the surface hardening layer. This article proposed an induction-heating method to produce gradient structure with a surface hardening layer of about 3 mm for the S38C steel to increase its mechanical performance. The strengthening mechanism and the variation of the microstructure were evaluated in detail. The operating process of the induction heating and quenching on the specimens was presented. After that, detailed microstructure analysis was conducted through electron backscatter diffraction (EBSD) to understand the variation of the gradient structure from surface to interior. Subsequently, small-scale tensile tests were performed to get the mechanical properties of the gradient structure in different depths, and full-scale tensile tests and the corresponding finite element simulation were conducted to examine the compatibility of the surface hardening layer and the core material, and analyze general mechanical behavior of the S38C steel with gradient structure. Finally, fatigue tests were performed to gain more understanding of the fatigue behavior of the surface hardening layer in HCF and very high cycle fatigue (VHCF) regimes, and the failure mechanism was also analyzed through microscopic study.

## 2. Experimental Section

### 2.1. Material

The as-received S38C steel material is obtained from an axle of a high-speed railway along the longitudinal direction, and it has chemical compositions (wt%) of 0.42 C, 0.26 Si, 0.76 Mn, 0.0056 P, 0.009 S, 0.02 Al, 0.0037 N, 0.0006 O, and balanced Fe. The original microstructure observed by an optical microscope is shown in **Figure 1**, which contains pearlite and coarse ferrite. The as-received S38C steel has a tensile strength of 643 MPa, and a hardness value of 201 HV.

### 2.2. Specimen Preparation and Induction Heat Treatment

The testing specimens were machined out from the as-received S38C steel, and their geometries are shown in **Figure 2a**. The longitudinal direction of the testing specimens is along with the longitudinal direction of the axle. Cylinder “A” in **Figure 2a** was treated by induction heating and quenching, as shown in **Figure 2b**. The treatment process parameters were identified after several trials for frequency and time. The treatment process started with induction heating at a frequency of 300 kHz for 45 s, and the surface temperature was 800 °C, and then water-based quenching fluid (a polymer quenching medium consisting mainly of polymer, biocide, activator, and water) was used to cool the cylinder. Finally, the cylinder was tempered at 220 °C for 1.5 h in a muffle furnace to reduce quenching stress and achieve a stable microstructure. In this way, the cylinder obtained the surface gradient structure, and it was used to collect the microstructural morphology and tensile properties of the gradient structure at different depths. As shown in **Figure 2c**, the tensile properties were obtained by fabricating small tensile specimens from the surface to the interior, which included the depths of 1.3, 2.6, 3.9, 5.2, 6.5, 7.8, 9.1, 10.4, 11.7, 13.0, and 14.3 mm. The longitudinal direction of the small tensile specimens was parallel with the longitudinal direction of cylinder “A”. Two or three specimens were prepared for each depth to ensure repeatability, and the small tensile specimens were cut by wire electrical discharge machining and were polished carefully to remove roughness and surface oxide.

Dog-bone specimen “B” and rotary bending fatigue specimen “C”, as shown in **Figure 2a**, were prepared for the tensile test and fatigue test, respectively. The two kinds of specimens were also treated by induction heating and quenching as introduced for

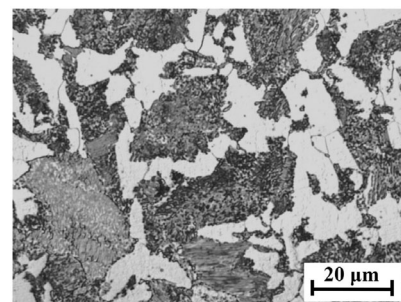


**Figure 1.** Microstructure of as-received S38C steel.

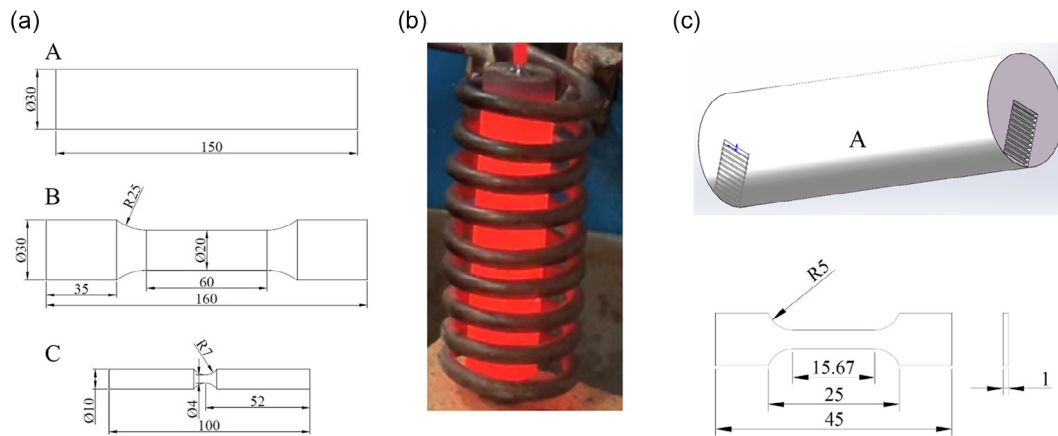


**Figure 2.** Testing specimens of S38C steel (all dimensions are in mm). a) Geometries of cylinder “A”, tensile specimen “B”, and rotary bending fatigue specimen “C”. b) Induction heating of cylinder “A”. c) Small-scale tensile specimens cut along longitudinal direction of cylinder “A”.

cylinder “A” to ensure that all the gradient structures have similar microstructure and hardness. After that, the gauge sections of the tensile specimens and fatigue specimens were polished carefully to remove surface oxidation and machining scratches.

### 2.3. Test Methods and Finite Element Analysis

The hardness of the specimens “A”, “B”, and “C” from surface to the core was measured by a microhardness tester with a load of 300 gf with a dwell time of 10 s to show the variation of the hardness of the gradient structure. The cross-section of cylinder “A” was polished to a mirror finish, and the microstructure at different depths was characterized by EBSD to understand the variation of the gradient structure.

The small-scale tensile specimens, as shown in Figure 2c, were used to examine the mechanical properties of the gradient structure at different depths, and uniaxial tensile tests for the specimens were conducted on an electric test machine Instron E3000 at a strain rate of  $10^{-4} \text{ s}^{-1}$ . The tensile specimen “B”, as shown in Figure 2a, was used to obtain general mechanical properties of the S38C steel with the gradient structure, and it was tested by servohydraulic test machine MTS 810 at a strain rate of  $10^{-4} \text{ s}^{-1}$ . Moreover, the tensile test of specimen “B” was simulated by a commercial finite element code LS-DYNA<sup>[31,32]</sup> to understand the strengthening behavior of the gradient structure and the failure characteristic. The specimen was modeled by solid elements, and the stress–strain parameters from surface to the core were defined according to the test results of small-scale tensile specimens in Figure 2c. A mesh size of about 0.8 mm was used, and a perfect bond was defined for different material layers. The specimen was modeled using an elastoplastic material model (MAT\_24), which was a common material model with a user-defined stress–strain curve. In the simulation, one side of the bar was fixed, and the other side was applied with a quasi-static loading.

The fatigue tests for specimen “C”, as shown in Figure 2a, were conducted on a rotary bending fatigue testing machine GIGA QUAD YRB200 with a loading frequency of 50 Hz and a stress ratio of  $-1$ .

After the tensile and fatigue tests, the fracture surfaces of the failed specimens were observed by a scanning electron microscope (SEM) to study fractography. For some fatigue specimens that failed from internal crack initiation, the crack origins were analyzed via energy dispersive spectroscopy (EDS) to identify chemical elements and determine whether they were inclusions or inhomogeneous microstructures. Subsequently, some foils were extracted in the internal crack initiation and early growth region by focused ion beam (FIB) technique. The microstructure of the foils was characterized by transmission Kikuchi diffraction (TKD) and transmission electron microscope (TEM) to understand the crack initiation mechanism.

## 3. Results and Discussion

### 3.1. Microstructural Properties of the Gradient Structure

The microstructure of cylinder “A” from surface to core was characterized by EBSD, and the band contrast maps and inverse pole figures (IPFs) at different depths are given in Figure 3a–g. Figure 3a,b shows tempered martensite microstructure at depths of 0.05 and 0.55 mm, respectively, which is obtained through the heat treatment introduced in Section 2.2. Subsequently, some fine pearlites appear in the tempered martensite microstructure at a depth of 5.5 mm from the surface, as shown in Figure 3c, and small colonies of ferrite and pearlite appear in the tempered martensite at depths of 6.5 mm to 10.0 mm, as shown in Figure 3d,e. At the depths of 13.9 and 14.5 mm (i.e., the core of cylinder “A”), as shown in Figure 3f,g, the microstructure becomes a mixture of pearlite, coarse ferrite, and tempered martensite. Meanwhile, the hardness of cylinder “A” from surface to core is shown in Figure 3i. Five independent values were measured for each depth, and the mean hardness values with error bars at each depth are given. It is found that the surface hardening layer has a hardness of about 700 HV, which is nearly triple that of the as-received state. It could be attributed to the strengthening effect of tempered martensite in the microstructure, as shown in Figure 3a,b. In the inner region from 2.6 mm, the hardness gradually decreases, and it becomes 300 HV at a depth of 14.0 mm.

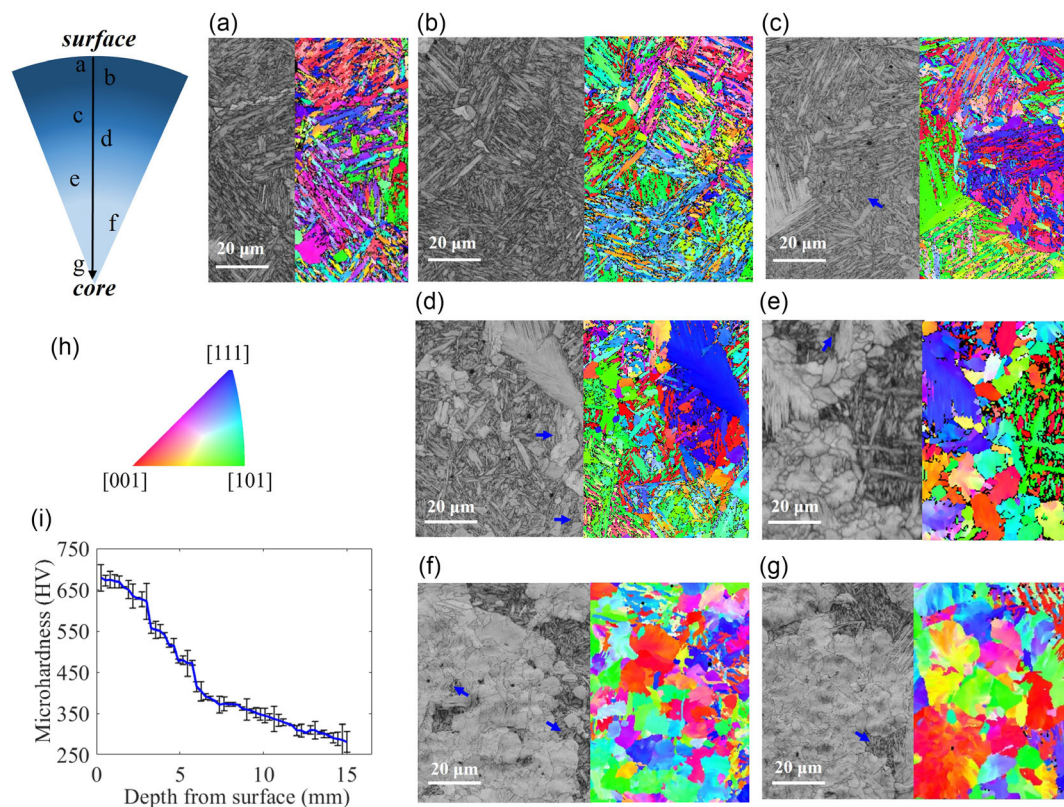


**Figure 3.** EBSD microstructural characterization of cylinder “A” from surface to core. Band contrast map and IPF at a) 0.05 mm, b) 0.55 mm, c) 5.5 mm, d) 6.5 mm, e) 10.0 mm, f) 13.9 mm, and g) 14.5 mm, respectively. h) Legend of IPF. i) Hardness of cylinder “A” from surface to core. Blue arrows in (c–g) denote pearlite.

The softer material should be attributed to the gain of pearlite and ferrite in the inner microstructure.

### 3.2. Tension Performance

#### 3.2.1. Tensile Properties of the Gradient Structure

The tensile properties of cylinder “A” at depths of 1.3, 2.6, 3.9, 5.2, 6.5, 7.8, 9.1, 10.4, 11.7, 13.0, and 14.3 mm were obtained via the tensile tests of the small-scale specimens. The average yield strength and average tensile strength of the steel at these depths are shown in **Figure 4a**, and the detailed engineering stress–strain curves of the tensile tests at depths of 2.6, 5.2, and 14.3 mm are shown in **Figure 4b,c,d**, respectively. It is found that the hardening layer from the surface to a depth of 2.6 mm has a tensile strength of about 2000 MPa, and the elongation at failure varied between 0.03 and 0.05. The high tensile strength and low maximum strain properties of the surface gradient structure were attributed to the tempered martensite microstructure. Subsequently, the tensile strength and yield strength decrease gradually, and then from a depth of 6.5 mm to the core, they keep about 650 and 360 MPa, respectively. However, according to **Figure 4b,c,d**, the elongation at failure gradually improves from surface to core. It should be attributed to the increase of pearlite and coarse ferrite in the microstructure.

#### 3.2.2. General Tensile Performance

The tensile test and finite element model for specimen “B” are shown in **Figure 5a,b**, respectively, which are used to examine the compatibility of the surface hardening layer and the core material, and analyze the general tensile performance of the S38C steel with gradient structure. **Figure 5c** shows the experimental stress–strain curve. It is seen that specimen “B” has a yield strength of 433 MPa, tensile strength of 1290 MPa, and maximum strain of 0.04. Accordingly, the steel after the induction heating and quenching presents a much higher tensile strength than that of the as-received material, but a brittle fracture behavior. The failure strain is close to the maximum strain of the surface hardening layer in **Figure 4b**, which indicates that failure is dominated by the surface gradient structure. Meanwhile, the hardness of specimen “B” from surface to core is measured to understand the variation of the gradient structure in specimen “B”, as shown in **Figure 6**. It indicates that the surface hardening layer has a depth of 2 mm from surface, in which the hardness keeps about 700 HV. Subsequently, the hardness gradually reduces from 700 to 300 HV in the depth (*x*-axis) from 2 to 5 mm, and keeps about 300 HV from 5 to 10 mm. Combining these results with the findings in **Figure 3i** and **4a**, specimen B has a surface hardening layer with a thickness of about 2 mm, followed by a strength-descent layer with a

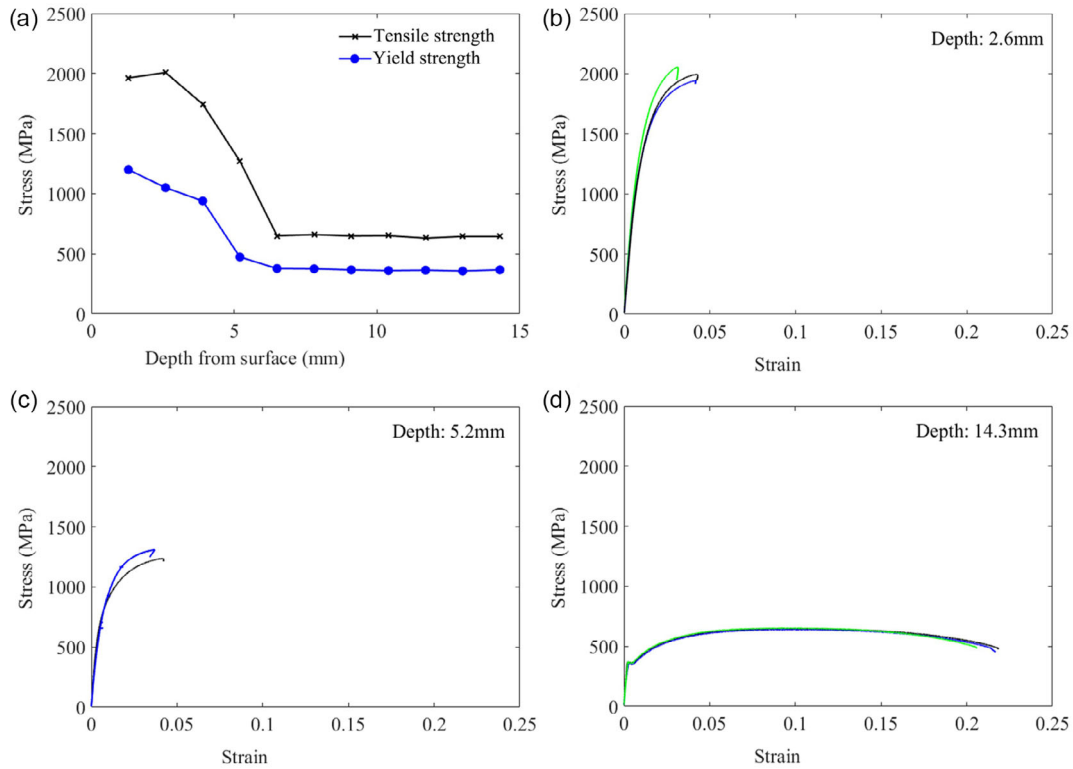


**Figure 4.** Tensile behavior of cylinder “A” at different depths. a) Variation of average yielding strength, and average tensile strength from surface to core. Stress–strain curves of the small-scale specimens at depths of b) 2.6 mm, c) 5.2 mm, and d) 14.3 mm, respectively.

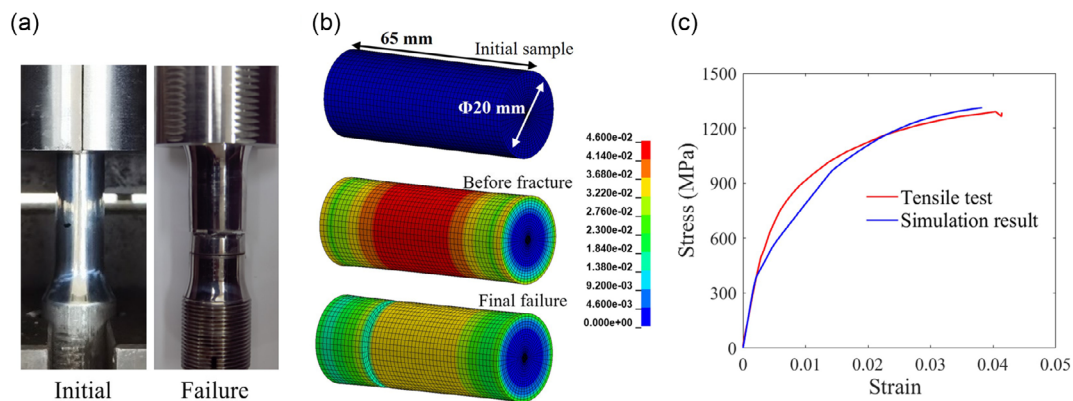


**Figure 5.** Tensile performance of the specimen “B” and corresponding finite-element result. a) Tensile testing images for the initial sample and after failure. b) Finite element model for the tensile test of specimen “B”. c) Stress–strain curves from the tensile test and finite element simulation.

thickness of about 3 mm, and relatively soft substrate material in the core.

The finite element model, as shown in Figure 5b, included three parts based on the hardness variation, as shown in Figure 6, and the mechanical behavior, as shown in Figure 4b–d, i.e., the outer hard layer with a thickness of 2 mm, the medium strength-descent layer with a thickness of 3 mm, and the inner soft core with a radius of 5 mm. The simulation result is shown in Figure 5c, and it presents good

consistency with the experimental stress–strain curve. The finite element contours of the equivalent plastic strain before and after fracture are presented in Figure 5b, which is consistent with the experimental observation in Figure 5a. The finite element model validates that the combination of the surface hardening layer with soft substrate material could significantly improve the tensile strength, and the failure strain highly depends on the surface hardening layer since the inner substrate material could not suffer such high loading.

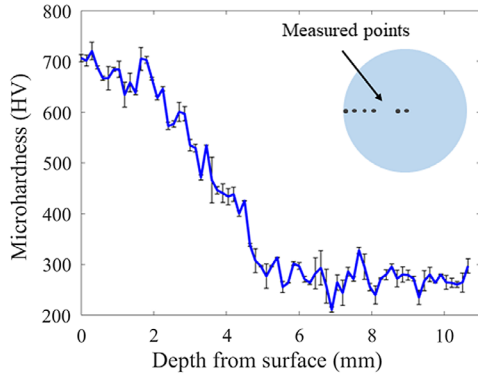


**Figure 6.** Hardness of the specimen “B” from surface to core.

### 3.3. Fatigue Performance

#### 3.3.1. S–N Data

Before the fatigue tests, the hardness of the minimum section of specimen “C” from surface to core was measured to examine the property of gradient structure in specimen “C”. As shown in **Figure 7a**, the hardness keeps about 740 HV from surface to a depth of 0.8 mm, and after that, the hardness gradually

decreases from 740 to 600 HV in the depth ( $x$ -axis) from 0.8 to 1.4 mm. In the depth of 1.4 to 2.0 mm (i.e., the core), the hardness remains at about 600 HV. Therefore, the hardness of the minimum section of specimen “C” is much higher than the initial state of S38C steel. **Figure 7b** shows a comparison of hardness from surface to core among the specimens “A”, “B”, and “C”, and it presents the general hardness of specimen “C” is close to the surface hardening layer of the specimens “A” and “B”. Therefore, after the induction heating and quenching, the whole minimum section of specimen “C” becomes a hardened layer, which could be used to study the fatigue behavior of the surface hardening layer.

**Figure 8a** shows the S–N data of the fatigue specimen “C”, and the fatigue life is prolonged as the stress amplitude reduces. The run-out specimen reaches fatigue cycles of  $6.3 \times 10^8$  under a stress amplitude of 750 MPa. The specimens with a shorter fatigue life (around  $1 \times 10^7$  cycles) tended to fail from surface crack initiation, while the specimens with a longer fatigue life tended to fail from internal crack initiation. Such fatigue crack initiation modes are similar to those reported for steel materials<sup>[33–35]</sup> and titanium alloys<sup>[36–38]</sup> and the fatigue life close to and in VHCF regime could promote the internal crack initiation. The number of data points of specimen “C” is a little small, and it is due to the limited specimens in the same batch.

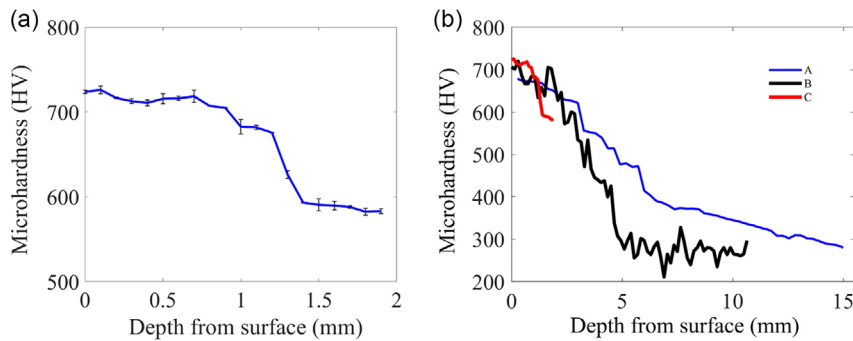


**Figure 7.** a) Hardness of the specimen “C” from surface to core. b) Comparison of hardness from surface to core among the specimens “A”, “B”, and “C”.

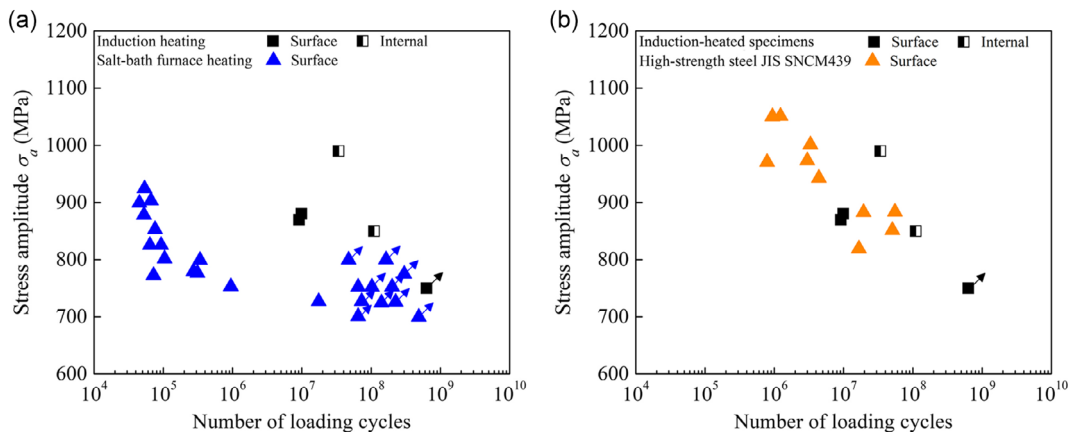


**Figure 8.** Comparison of S–N data. a) Between the present S38C steel with the gradient structure and the S38C steel treated by salt-bath furnace heating in the study of Jiang.<sup>[22]</sup> b) Between the present S38C steel with the gradient structure and high-strength steel JIS SNCM439 in the study of Furuya et al.<sup>[39]</sup> Reproduced with permission.<sup>[39]</sup> Copyright 2002, Elsevier.

Moreover, S–N data of a group of the S38C specimens treated by salt-bath furnace heating in the study of Jiang<sup>[22]</sup> and S–N data of high-strength steel JIS SNCM439 in the study of Furuya et al.<sup>[39]</sup> are given in Figure 8a,b, respectively, to compare with the results of the present induction-heated specimens. The S38C specimens treated by salt-bath furnace heating have a surface hardness of 557 HV. It is seen that the induction-heated specimens in the present study show much longer fatigue life under the stress amplitude of 850 to 990 MPa. The superior fatigue behavior indicated a better strengthening effect by the induction heating and quenching in Section 2.2. In Figure 8b, the fatigue performance of the present fatigue specimens is comparable with that of high-strength steel JIS SNCM439. The JIS SNCM439 steel owns a tempered martensitic microstructure and its tensile strength reaches 1955 MPa.<sup>[39]</sup> Overall, these fatigue results indicate that the induction heat treatment could provide an effective surface hardening layer for the S38C steel to improve the surface strength and inhibit surface crack initiation.

### 3.3.2. Fatigue Fracture Surface

The specimens that failed from surface crack initiation and internal crack initiation are shown in Figure 8a,b, and c,d, respectively. Surface crack initiation is common in fatigue tests, and it could be due to the stress concentration in surface under cyclic loading.<sup>[40]</sup> The internal crack initiation mode in Figure 8d presents a fish-eye feature and the crack initiates from a subsurface inclusion, and the fish-eye feature is a characteristic region for crack initiation and early growth in VHCF regime. This crack initiation mode is similar to those steel materials that failed in VHCF regime.<sup>[22,33,35]</sup> Therefore, the crack initiation of the induction-heated S38C specimens in VHCF regime could be induced at the surface or around subsurface inclusion. However, the crack growth regions for both surface and internal crack initiation modes in Figure 8a,c are quite narrow, which are different from usually noticed significant crack growth regions on fatigue fracture surfaces of steel materials.<sup>[33,35]</sup> It could be due to that the gradient structure has significantly improved

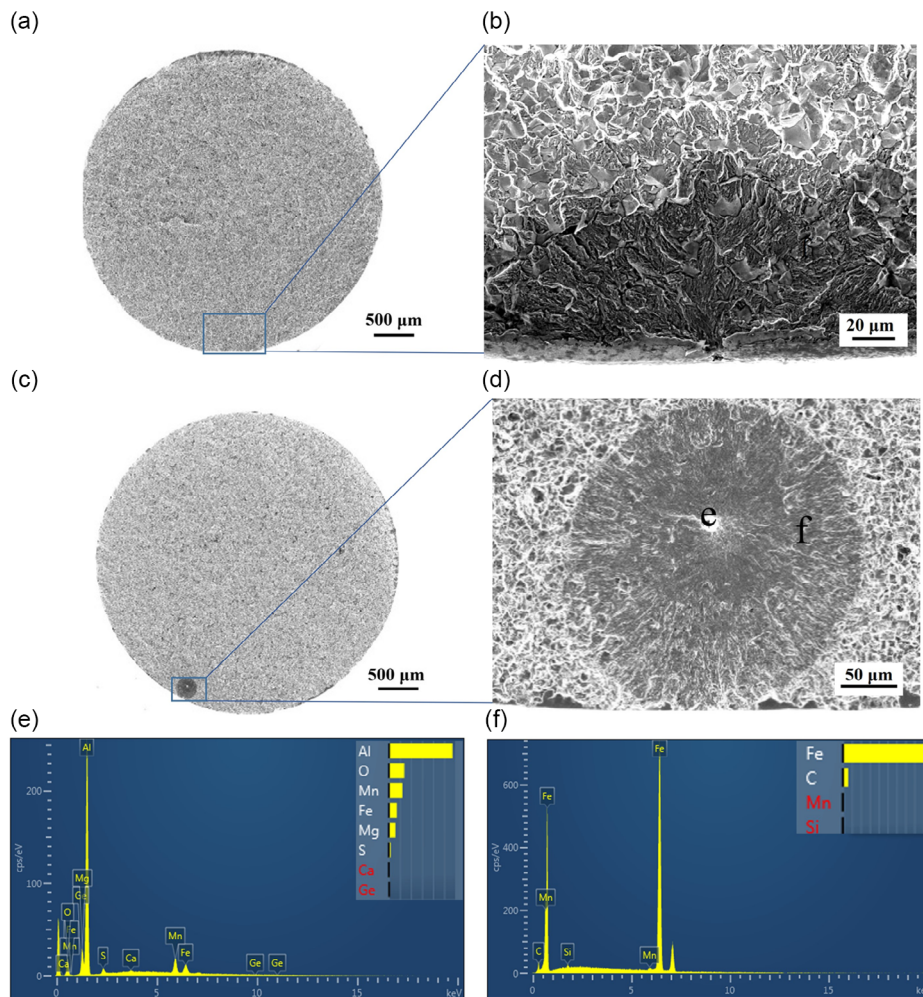


**Figure 9.** Fracture surface of the failed specimens. a,b) Surface crack initiation,  $\sigma_a = 870$  MPa, and  $N_f = 9.1 \times 10^6$  cycles, b) a magnified view of the crack initiation region in (a). c,d) Internal crack initiation with fish-eye feature,  $\sigma_a = 850$  MPa, and  $N_f = 1.1 \times 10^8$  cycles, d) a magnified view of the crack initiation region in (c). EDS analysis for e) the inclusion and f) substrate material in the fish-eye region.

the fatigue loading capacity, but once the crack grows a little in the specimens, they could not suffer such a high loading and would fail soon.

Furthermore, the compositions of the inclusion and the substrate material in the fish-eye region in Figure 8d are analyzed by EDS to understand the crack initiation behavior, and the elemental analysis results are shown in Figure 8e,f, respectively. It is found that the inclusion is almost a nonmetallic compound, which contains high-level of Al and O, followed by Mn, Mg, and S. It indicates that the main components of the inclusions could be  $\text{Al}_2\text{O}_3$ , FeO, MnO, MgO, MnS, within which  $\text{Al}_2\text{O}_3$  is the highest. The substrate material in the fish-eye region is still Fe and C.

### 3.3.3. Microscopic Study of Internal Crack Initiation

Since the internal crack initiation region in Figure 9c is near the surface and in the gradient structure, a microscopic study including TKD and TEM characterization is conducted for the

microstructure in this region to understand the internal crack initiation mechanism in the gradient structure. A foil is extracted in position I near the inclusion via FIB technology, as shown in Figure 10a,b–d, which gives IPF, phase map, and kernel average misorientation (KAM) image of the foil, respectively. It is seen that the nanograins are discontinuously distributed along the surface, and the average KAM values for the nanograin regions are relatively higher than those of the coarse grains nearby. Therefore, the nanograins could be caused by local high-stress concentration around the inclusion in the gradient structure as well as dislocation accumulation and interaction in the nearby grains during the cyclic loading process.<sup>[36,37]</sup> Further, microcracks form around the inclusion and the nanograins, and gradually coalesce as well as grow up to conventional cracks to induce fatigue failure.

The foil is also observed by TEM in the crack initiation region, and selected area diffraction (SAD) is used to further identify the microstructure characteristics. The nanograins can be seen near the fracture surface in Figure 11a, and the SAD pattern of

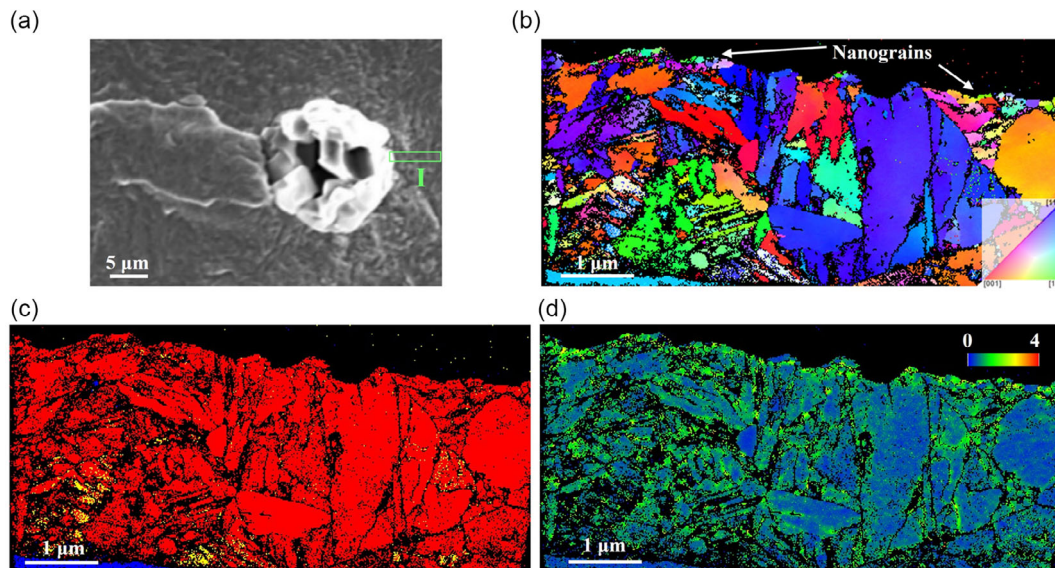


**Figure 10.** SEM and TKD characterization for the microstructures in the internal crack initiation region,  $\sigma_a = 850$  MPa, and  $N_f = 1.1 \times 10^8$  cycles. a) SEM image for the position I near the inclusion. b) IPF, c) phase map, and d) KAM image of the extracted foil in position I.

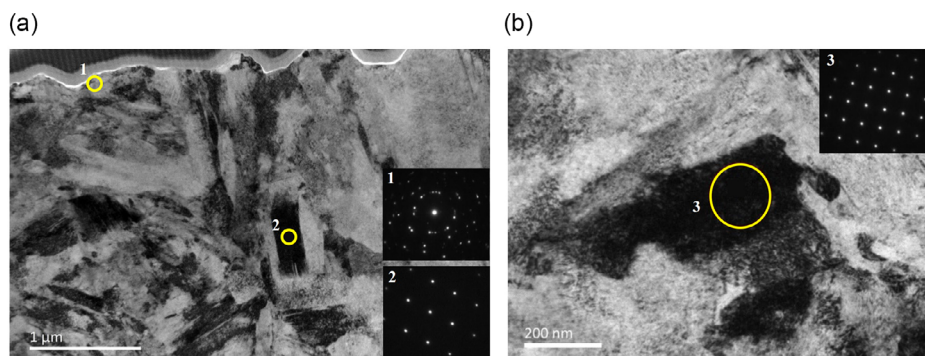


**Figure 11.** TEM observation on the microstructures of the extracted foil. a) Bright-field image of the foil. b) Grains away from the fracture surface. Insets in (a) and (b) are SAD patterns of the associated circular regions.



circular region 1 in Figure 11a shows many tiny dots placed as discontinuous rings which further confirm the nanograins below the fracture surface. In the region away from the fracture surface, the SAD patterns of circular regions 2 and 3 in Figure 11a,b are isolated diffraction points, i.e., single crystal diffraction features.

The induction-heating method proposed in this article has the advantages of easy operation and a good strengthening effect. The detailed characterization of the gradient structure in Section 3.1 provided a direct view of the variation of microstructure for the S38C steel with gradient structure, and the corresponding small scale-tensile tests presented the variation of mechanical performance of the gradient structure in different depths. These studies provided an important understanding of the strengthening mechanism, viz., the surface gradient structure of the S38C steel became a dominant bearing part. The results in Section 3.2 and 3.3 indicated that the surface gradient structure produced by the induction heating greatly improved the tensile strength and fatigue performance of the S38C steel. Moreover, the hardness of the surface gradient structure with tempered martensite reaches about 700 HV, which is much harder than the gradient structure of S38C steel (about 500–600 HV) in the literature.<sup>[15,18,22,41]</sup> Therefore, the steel with gradient structure developed in this study could be used for the components requiring high strength and good fatigue resistance.

## 4. Conclusion

This article proposed an induction heating and quenching method to fabricate the gradient structure for S38C steel. The strengthening mechanism and failure mechanism were studied using microscopic characterization and finite element analysis in detail. The main conclusions are summarized as follows: 1) the surface gradient structure fabricated by the induction heating and quenching was tempered martensite microstructure, which obviously improved the hardness and tensile strength of surface and subsurface regions. 2) This surface gradient structure significantly increased the tensile strength of the S38C steel, and it became a dominant part of suffering loading. 3) The surface hardening layer possessed a high fatigue strength, which was higher than the S38C specimens treated by salt-bath furnace heating and was close to that of high-strength steel. The strengthening effect of the induction heating and quenching was superior to the salt-bath furnace heating and quenching. 4) The fatigue failure of the surface hardening layer could be due to local stress concentration on the surface and around subsurface inclusions, and the crack initiation modes present surface crack initiation and internal crack initiation, respectively.

## Acknowledgements

The authors gratefully acknowledge the support of the National Natural Science Foundation of China Basic Science Center for “Multiscale Problems in Nonlinear Mechanics” (No.11988102). The authors are grateful to Prof. Yujie Wei for his suggestions in the experiments.

## Conflict of Interest

The authors declare no conflict of interest.

## Author Contributions

G.L.: Conceptualization, methodology, data analysis, investigation, writing–review and editing, funding acquisition. L.Z.: Data analysis, investigation, writing–review and editing. Q.J.: Investigation, writing–review and editing. Y.W.: Investigation, writing–review and editing. R.G.: Investigation, writing–review and editing. Z.M.: Conceptualization, methodology, data analysis, investigation, writing–review and editing, funding acquisition.

## Data Availability Statement

The data that support the findings of this study are available from the corresponding author upon reasonable request.

## Keywords

fatigue performance, gradient structures, induction heating and quenching, medium carbon steels, tension performance

Received: June 15, 2023

Revised: September 17, 2023

Published online: October 15, 2023

- [1] Y. Wei, Y. Li, L. Zhu, Y. Liu, X. Lei, G. Wang, Y. Wu, Z. Mi, J. Liu, H. Wang, *Nat. Commun.* **2014**, *5*, 1.
- [2] T. Fu, Z. F. Zhou, Y. M. Zhou, X. D. Zhu, Q. F. Zeng, C. P. Wang, K. Li, J. Lu, *Surf. Coat. Technol.* **2012**, *207*, 555.
- [3] C. W. Shao, P. Zhang, Y. K. Zhu, Z. J. Zhang, Y. Z. Tian, Z. F. Zhang, *Acta Mater.* **2018**, *145*, 413.
- [4] X. Wu, P. Jiang, L. Chen, F. Yuan, Y. Zhu, in *Heterostructured Materials*, Jenny Stanford Publishing, Dubai, UAE **2021**, pp. 53–71.
- [5] W. Chen, Z. S. You, N. R. Tao, Z. H. Jin, L. Lu, *Acta Mater.* **2017**, vol. *125*, pp. 255.
- [6] R. O. Ritchie, *Nat. Mater.* **2011**, *10*, 817.
- [7] K. Lu, *Science* **2014**, *345*, 1455.
- [8] Z. W. Ma, J. B. Liu, G. Wang, H. T. Wang, Y. J. Wei, H. J. Gao, *Sci. Rep.* **2016**, *6*, 11.
- [9] R. Fajkos, R. Zima, B. Strnadel, *Fatigue Fract. Eng. Mater. Struct.* **2015**, *38*, 1255.
- [10] J. W. Gao, M. H. Yu, D. Liao, S. P. Zhu, J. Han, G. Lesiuk, J. Correia, A. M. P. De Jesus, *Int. J. Fatigue*, **2021**, *149*, 8.
- [11] Y. A. Hu, Q. B. Qin, S. C. Wu, X. Zhao, W. J. Wang, *Int. J. Fatigue*, **2021**, *144*, 10.
- [12] H. Zhang, S. C. Wu, N. Ao, J. W. Zhang, H. Li, L. Zhou, P. G. Xu, Y. H. Su, *Int. J. Fatigue*, **2023**, *166*, 11.
- [13] Y. Luo, T. Y. Qin, X. Jia, Y. X. Hu, C. H. Li, G. Y. Mu, S. C. Wu, *Eng. Fail. Anal.* **2022**, *142*, 16.
- [14] Y. Zhang, Z. Han, K. Wang, K. Lu, *Wear* **2006**, *260*, 942.
- [15] Y. Wang, L. C. Yuan, S. J. Zhang, C. Q. Sun, W. J. Wang, G. X. Yang, Q. Li, Y. J. Wei, *Eng. Fract. Mech.* **2019**, *209*, 369.
- [16] U. Zerbst, C. Klinger, D. Klingbeil, *Eng. Fail. Anal.*, **2013**, *35*, 54.
- [17] K. Lu, *Nat. Rev. Mater.* **2016**, *1*, 13.
- [18] J. W. Gao, X. N. Pan, J. Han, S. P. Zhu, D. Lia, Y. B. Lio, G. Z. Dai, *Int. J. Fatigue* **2020**, *139*, 11.
- [19] W. C. Liu, G. H. Wu, C. Q. Zhai, W. J. Ding, A. M. Korsunsky, *Int. J. Plast.*, **2013**, *49*, 16.
- [20] K. Lu, J. Lu, *J. Mater. Sci. Technol.* **1999**, *15*, 193.
- [21] W. L. Li, N. R. Tao, K. Lu, *Scr. Mater.* **2008**, *59*, 546.
- [22] Q. Q. Jiang, Dissertation, University of Chinese Academy of Sciences, **2017**.

- [23] T. H. Fang, W. L. Li, N. R. Tao, K. Lu, *Science* **2011**, 331, 1587.
- [24] L. Yang, N. R. Tao, K. Lu, L. Lu, *Scr. Mater.* **2013**, 68, 801.
- [25] T. Roland, D. Reiraint, K. Lu, J. Lu, *Scr. Mater.* **2006**, 54, 1949.
- [26] S. Liu, B. Wang, P. Zhang, X. Bai, Q. Q. Duan, X. G. Wang, Z. F. Zhang, *Steel Res. Int.* **2022**, 93, 6.
- [27] O. Lucia, P. Maussion, E. J. Dede, J. M. Burdío, *IEEE Trans. Ind. Electron.* **2014**, 61, 2509.
- [28] Z. W. Ma, Y. Ren, R. G. Li, Y. D. Wang, L. L. Zhou, X. L. Wu, Y. J. Wei, H. J. Gao, *Mater. Sci. Eng. A Struct. Mater. Prop. Microstruct. Process.* **2018**, 712, 358.
- [29] Z. Zeng, X. Y. Li, D. S. Xu, L. Lu, H. J. Gao, T. Zhu, *Extreme Mech. Lett.* **2016**, 8, 213.
- [30] N. R. Tao, Z. B. Wang, W. P. Tong, M. L. Sui, J. Lu, K. Lu, *Acta Mater.* **2002**, 50, 4603.
- [31] G. Li, L. Ke, W. J. Peng, X. C. Ren, C. Q. Sun, *Theor. Appl. Fract. Mech.* **2022**, 119, 10.
- [32] G. Li, K. H. Tan, T. C. Fung, Q. J. Yu, M. May, *Compos. Struct.* **2021**, 268, 113872.
- [33] G. Li, L. Ke, W. Peng, X. Ren, C. Sun, *Theor. Appl. Fract. Mech.* **2022**, 119, 103360.
- [34] H. Kobayashi, A. Todoroki, T. Oomura, T. Sano, T. Takehana, *Int. J. Fatigue* **2006**, 28, 1633.
- [35] M. L. Zhu, F. Z. Xuan, Y. N. Du, S. T. Tu, *Int. J. Fatigue* **2012**, 40, 74.
- [36] G. Li, L. Ke, X. Ren, C. Sun, *Int. J. Fatigue* **2022**, 166, 107299.
- [37] G. Li, C. Q. Sun, *J. Mater. Sci. Technol.*, **2022**, 122, 128.
- [38] X. L. Liu, C. Q. Sun, Y. S. Hong, *Mater. Sci. Eng. A Struct. Mater. Prop. Microstruct. Process.* **2015**, 622, 228.
- [39] Y. Furuya, S. Matsuoka, T. Abe, K. Yamaguchi, *Scr. Mater.* **2002**, 46, 157.
- [40] M. C. Ding, Y. L. Zhang, H. T. Lu, *Int. J. Fatigue* **2020**, 139, 10.
- [41] J. W. Gao, M. H. Yu, D. Liao, S. P. Zhu, Z. Y. Zhu, J. Han, *Mater. Des.* **2021**, 202, 10.